European Journal of Mechanics / A Solids 96 (2022) 104678

Contents lists available at ScienceDirect

European Journal of Mechanics / A Solids

journal homepage: www.elsevier.com/locate/ejmsol

Dynamics of vehicle stability control subjected to feedback delay

Hangyu Lu [a,b], Gabor Stepan [b,*], Jianwei Lu [a], Denes Takacs [b,c]

[a] School of Automotive and Transportation Engineering, Hefei University of Technology, Hefei, 230000, Anhui Prov., China
[b] Department of Applied Mechanics, Faculty of Mechanical Engineering, Budapest University of Technology and Economics, Budapest, H-1111, Hungary
[c] MTA-BME Research Group on Dynamics of Machines and Vehicles, Budapest, H-1111, Hungary

ARTICLE INFO

Keywords:
Delay
Vehicle lateral stability
Phase plane analysis
Stability chart
Optimised control
Global stability

ABSTRACT

Mechanical systems with feedback control commonly contain time delays which usually tend to destabilise the system. With increasing accuracy requirements of data acquisition and calculation, investigation of the effect of the feedback delay including the computational time, actuating time, and signalling time is crucial for developing advanced chassis control. A 2-dimensional vehicle handling model with feedback control torque is introduced to analyse the dynamics of vehicle stability control system. A revised version of the PAC-2002 tyre model is used to create two qualitatively different steering characteristics by tuning the contact friction coefficients at the front and rear wheels. The stability charts in the space of the control gains are constructed. In understeer and oversteer cases, the control gains are optimised to achieve the fastest settling signals against small perturbations. While the optimised gains provide global stability of the cornering manoeuvres in the oversteer case, the gains should be further tuned in the understeer case to ensure fast settling signals and also global stability. The optimisation procedure is presented for various realistic time delays.

1. Introduction

When time delay occurs in mechanical systems, the rate of change of state variables is determined by both past and present state variables (Insperger and Stepan, 2011). Vehicle, as a typical integrated complex system, also cannot avoid the existence of various types of time delays. In the dynamics of vehicle handling, time delays are mainly caused by the reaction delay of the human driver, the time lag in the steering assembly, and the propagation of the transient deformation appearing in the elastic tyre–road contact. These delays lead to various stability problems in cornering manoeuvrability (Rossa and Mastinu, 2017), in high-speed steerability (Wu et al., 2019), in traffic jam formation (Orosz and Stepan, 2006; Sipahi et al., 2008), and even in inducing wheel shimmy (Takacs and Stepan, 2012).

Vehicles are equipped with more and more active and intelligent controls to reduce the risk of accidents and to save lives (Olofsson and Nielsen, 2021), but the time delays existing in the control loops still weaken the global performance of these systems and may even carry safety concerns as shown in the analyses of longitudinal force control (Horvath et al., 2021), automated vehicle steering control (Oh et al., 2021; Várszegi et al., 2019), drifting control for path following (Goh et al., 2019), and lane-keeping control (Xu et al., 2021).

To analyse such delayed systems, the characterisation of their local behaviour around a desired position or a desired path is required, and the results can be summarised in stability charts presenting the stability of the linearised system in the space of selected system parameters (Hu and Wang, 2002). This provides a useful tool to optimise the control parameters in the presence of time delays and to support the practical process of tuning the gains.

Vehicle stability control systems that typically employ feedback control require the acquisition of real-time vehicle state (Singh et al., 2018). Today's stability control systems based on the direct-yaw-moment control theory, such as ESC (Electronic stability control) and ABS (Anti-lock braking system), activate the torque control when the controlled state exceeds a certain threshold (Takahashi et al., 2012). Some time delay always appears in such activation processes. Advanced chassis stability control systems, especially in intelligent and unmanned vehicles, require high accuracy and additional parameters in vehicle state estimations to enhance safety, that include, for example, tyre force estimation and/or road profile estimation. With the implementation of these sophisticated high dimensional vehicle models (Zhao et al., 2018) and non-linear tyre models (Acosta et al., 2018), or with the applied complex algorithms like the non-linear Kalman filter (Nam et al., 2011) and non-linear observers (Chen et al., 2014), relatively large delay is generated in the process due to the high computational costs. Apart from these computational costs, the signalling time of the sensors and the actuating time of the mechanical actuators are also non-negligible in real engineering applications (Patole et al., 2017; Sridhar

* Corresponding author.
E-mail addresses: hangyulu@mm.bme.hu (H. Lu), stepan@mm.bme.hu (G. Stepan), jwlu75@hfut.edu.cn (J. Lu), takacs@mm.bme.hu (D. Takacs).

https://doi.org/10.1016/j.euromechsol.2022.104678
Received 15 February 2022; Received in revised form 25 May 2022; Accepted 29 May 2022
Available online 8 June 2022

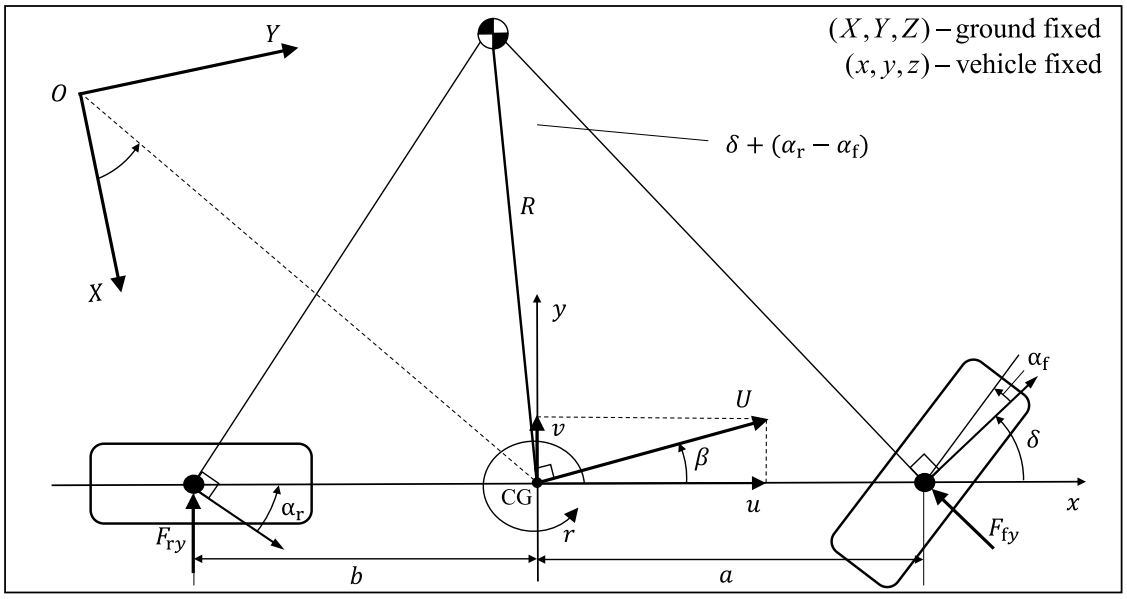

Fig. 1. Vehicle handling model considering yaw and lateral side-slip.

et al., 2021; Miller and Cebon, 2013), and consequently, they should be considered and identified when developing a system in practice.

In simulations, time delay is often incorporated in the filtering update or in the observation process while the optimisation of the control parameters takes place iteratively (Pi et al., 2011; Verma et al., 2015; Doumiati et al., 2011). Nevertheless, the global asymptotic stability of the closed-loop system has to be ensured even in the presence of time delays. In the space of the control parameters, the so-called stability charts can take into account the effects of the time delays, and consequently, they support the optimisation process and the corresponding tuning of the gains during the development of advanced chassis control systems.

This paper investigates a classical proportional feedback torque controller (Lugner, 2019) in Vehicle Stability Control (VSC) as an example to show the effect of time delay. Two different steering characteristics, understeer and oversteer, are considered in comparison. For small perturbations, the ζ-optimisation is conducted to select the gains for the fastest settling signals by extending the previous results in Boussaada et al. (2020) and Wang and Wang (2017), while for large perturbations, the optimisation is conducted to guarantee also the global stability of the system. Numerical simulations are carried out with the optimised control gains in order to check the local and global dynamic behaviour of the controlled system by means of inspecting the time history of the state variables and also by analysing the phase plane structure. Finally, the concluding section summarises the main contributions.

2. Dynamic model of vehicle handling

The governing equations are based on a single track vehicle model, which is also called bicycle model. Two coordinate systems are used, the ground fixed (X, Y, Z) and the local (x, y, z) that is fixed to the vehicle as shown in Fig. 1. The vehicle is considered to be rigid with the steering angle δ fixed in time. The vehicle motion is characterised by the velocity vector **U** of its centre of gravity CG, where its lateral component is the state variable v, while the longitudinal component u is constrained to be constant; the other state variable is the yaw rate r about the vertical axis Z.

2.1. Vehicle model

Fig. 1 presents the mechanical model in question. The vehicle mass is denoted by m, and the mass moment of inertia w.r.t the Z axis at CG is I_z. The distances from CG to the front and rear axles are given by a and b, respectively. The input steering angle δ is measured at the front axle relative to the vehicle body. The front and rear lateral tyre-ground interaction forces are denoted by $F_{\mathrm{f}y}$ and $F_{\mathrm{r}y}$, respectively. The equations of motion assume the form Pacejka (2005):

$$\begin{aligned} \dot{v} &= \frac{1}{m}\left(F_{\mathrm{f}y}(\alpha_{\mathrm{f}})\cos\delta + F_{\mathrm{r}y}(\alpha_{\mathrm{r}})\right) - ur\,, \\ \dot{r} &= \frac{1}{I_z}\left(aF_{\mathrm{f}y}(\alpha_{\mathrm{f}})\cos\delta - bF_{\mathrm{r}y}(\alpha_{\mathrm{r}})\right). \end{aligned} \tag{1}$$

The tyre-ground kinematic relations define the corresponding tyre side slip angles:

$$\alpha_{\mathrm{f}} = \delta - \arctan\left(\frac{v + ar}{u}\right), \quad \alpha_{\mathrm{r}} = -\arctan\left(\frac{v - br}{u}\right), \tag{2}$$

which are used to calculate the lateral tyre forces $F_{\mathrm{f}y}$ and $F_{\mathrm{r}y}$ with the help of an appropriate tyre model to be presented in the next subsection. The parameters listed in Table 1 are taken from a classical urban SUV car.

Table 1
Tested vehicle parameters.

Parameter	Symbol	Value	Unit
Vehicle mass	m	1475	kg
Yaw inertia	I_z	2400	kg m^2
Distance from COG to front axle	a	1.206	m
Distance from COG to rear axle	b	1.434	m
Wheel base	l	2.640	m

2.2. Modelling tyre force

Modelling the elastic tyre forces is always a crucial part of vehicle dynamics due to its strong nonlinearity generated at the tyre–road interaction. The so-called Magic Formula tyre model, put forward by Pacejka in 1989, is considered for modelling tyre–road interaction forces in applications (Pacejka, 2005). Its latest version, the PAC-2002 tyre model (Kuiper and Van Oosten, 2007) is applied in this paper to calculate the lateral forces:

$$F_y = D_y \sin\Big(C_y \arctan\big(B_y\alpha - E_y(B_y\alpha - \arctan(B_y\alpha))\big)\Big). \tag{3}$$

The detailed definitions and explanations of the coefficients are listed in Appendix together with the identified value of tyre parameters (see Table 2 in Appendix).

The vertical load F_z is calculated for the front and rear axles separately, and these are assumed to be the constant values

$$F_{fz} = \frac{b}{l}mg\,,\quad F_{rz} = \frac{a}{l}mg\,, \tag{4}$$

that is, the dynamic load transfer effect is neglected here. The tyre characteristic data were acquired through MTS Flat-Trac CT experiments for the tyre Giti 225/55R18 98v, and then they were fitted into the tyre model through genetic optimisation algorithm that finally presented the required parameters in Table 2.

3. Delayed feedback control of cornering manoeuvres

As it is discussed in the literature (see, for example, Lugner, 2019), in understeer cases, perturbations lead to the loss of grip force at the front wheel first: the yaw rate of the vehicle decreases due to the lack of the balance of the front and rear grip forces, while the body lateral speed does not change much:

$$\begin{cases} v \approx v_0 \approx 0, \quad e_v = v - v_0 \approx 0\,, \\ r_0 > r > 0, \quad e_r = r - r_0 < 0\,, \end{cases} \tag{5}$$

where e_v and e_r denote the corresponding state errors.

For oversteer cases, the perturbations result in the loss of the rear grip force first, which leads to an excessive body yaw rate that also gives in return an increased (negative) body lateral speed:

$$\begin{cases} v < v_0 \approx 0, \quad e_v = v - v_0 < 0\,, \\ r > r_0 > 0, \quad e_r = r - r_0 > 0\,. \end{cases} \tag{6}$$

To avoid these situations, recent chassis stability control systems such as ESC or VSC aim to keep the vehicle in a desired stable state and generate an appropriate dynamic response to the driver's inputs by individually braking the specific left and right wheels, and consequently, producing an additional yaw moment.

In the bicycle model, this yaw moment is taken into account by means of the classical feedback torque controller with proportional gains K_v and K_r over the state errors e_v and e_r, respectively, in the form

$$M_z(t) = K_v(v(t-\tau) - v_0) - K_r(r(t-\tau) - r_0)\,, \tag{7}$$

where the unavoidable time delay τ also appears in the feedback control loop for the practical reasons explained in the Introduction. In order to complete the mathematical model, the control torque (7) should appear on the right-hand-side of the second equation of the governing Eqs. (1).

4. Dynamics of delayed stability control for lane-keeping with small steering angles

In this section, the vehicle model in (1) is completely linearised by assuming small steering angle as in case of lane-keeping, and the tyre forces are also linearised for small side slip angles as they follow the linear relation

$$F_{fy} = C_f\alpha_f,\quad F_{ry} = C_r\alpha_r \tag{8}$$

with cornering stiffnesses $C_f = K_{fy}$, $C_r = K_{ry}$ obtained from (3) and (A.5) (see Appendix). Accordingly, the linearisation of the equations of motions (1) results in

$$\begin{aligned} m\dot{v} + \frac{C_f + C_r}{u}v + \left(mu + \frac{C_f a - C_r b}{u}\right)r = C_f\delta\,, \\ I\dot{r} + \frac{C_f a^2 + C_r b^2}{u}r + \frac{C_f a - C_r b}{u}v = C_f a\delta\,. \end{aligned} \tag{9}$$

In steady-state steering of this linear model, the steering characteristics are determined by

$$\begin{aligned} C_f a - C_r b > 0 \quad &\Rightarrow \quad \text{oversteer}\,, \\ C_f a - C_r b < 0 \quad &\Rightarrow \quad \text{understeer}\,. \end{aligned} \tag{10}$$

as already derived in Pacejka (2005) and Rossa et al. (2012).

When the input δ and u are given constant values, the trivial solutions assume the form

$$\begin{cases} r_0 = \dfrac{C_f C_r l u}{C_f C_r l^2 - (C_f a - C_r b)mu^2}\delta\,, \\ v_0 = \dfrac{(C_f C_r l b - mu^2 C_f a)u}{C_f C_r l^2 - mu^2(C_f a - C_r b)}\delta\,. \end{cases} \tag{11}$$

In order to investigate the stability around this equilibrium, the small perturbations $\xi(t) = v(t) - v_0$ and $\eta(t) = r(t) - r_0$ are introduced and substituted into the equation of motion (9) resulting

$$\dot{\mathbf{x}}(t) = \mathbf{A}\mathbf{x}(t)\,, \tag{12}$$

where $\mathbf{x} = [\xi\ \eta]^T$, and the coefficient matrix assumes the form

$$\mathbf{A} = -\begin{bmatrix} \dfrac{C_f + C_r}{um} & u + \dfrac{C_f a - C_r b}{um} \\ \dfrac{C_f a - C_r b}{uI_z} & \dfrac{C_f a^2 + C_r b^2}{uI_z} \end{bmatrix}. \tag{13}$$

The stability of the trivial solutions is determined by the eigenvalues λ_j $(j = 1, 2)$ of the coefficient matrix $\mathbf{A}$. These satisfy the characteristic equation

$$\lambda^2 - b_0\lambda + c_0 = 0\,, \tag{14}$$

where $b_0 = \mathrm{Tr}\mathbf{A}$ is easily found to be negative and

$$c_0 = \det\mathbf{A} = \frac{C_f C_r l^2}{I_z mu^2}\left(1 - mu^2\frac{C_f a - C_r b}{C_f C_r l^2}\right). \tag{15}$$

According to the Routh–Hurwitz criterion, the steady-state motion is exponentially stable if and only if $b_0 < 0$ and $c_0 > 0$. The first condition always fulfils, while regarding the second condition, there exists a critical speed limit u_{cr} for oversteered vehicles leading to the loss of stability, that is, when

$$u > u_{cr} = \sqrt{\frac{C_f C_r l^2}{m(C_f a - C_r b)}}\,. \tag{16}$$

One can show that the steady-state motion is always stable locally in understeer cases.

By including the linear delayed control torque (7), the completely linearised system can be rewritten in the form of a delay differential equation (DDE):

$$\begin{aligned} &m\dot{v}(t) + \frac{C_f + C_r}{u}v(t) + \left(mu + \frac{C_f a - C_r b}{u}\right)r(t) = C_f\delta\,, \\ &I_z\dot{r}(t) + \frac{C_f a^2 + C_r b^2}{u}r(t) + \frac{C_f a - C_r b}{u}v(t) = \\ &\qquad C_f a\delta + K_v(v(t-\tau) - v_0) - K_r(r(t-\tau) - r_0)\,, \end{aligned} \tag{17}$$

where both the tyre model and the vehicle model are linearised.

4.1. Stability criterion for the completely linearised model with delay effect

The equilibrium point (11) of the system is not affected by controller (7). Then the governing Eqs. (17) assume the form of linear autonomous DDEs :

$$\dot{\mathbf{x}}(t) = \mathbf{A}\mathbf{x}(t) + \mathbf{B}\mathbf{x}(t-\tau)\,, \tag{18}$$

where the coefficient matrix $\mathbf{A} = [a_{ij}]$ $(i, j = 1, 2)$ remains the same as in (13), while

$$\mathbf{B} = \begin{bmatrix} 0 & 0 \\ k_v & -k_r \end{bmatrix} \quad \text{with} \quad k_v = \frac{K_v}{I_z},\ k_r = \frac{K_r}{I_z}\,. \tag{19}$$

The characteristic equation is obtained from

$$\det(\lambda\mathbf{I} - \mathbf{A} - \mathbf{B}e^{-\lambda\tau}), \tag{20}$$

which gives

$$D(\lambda) := \lambda^2 - b_0\lambda - (a_{11}k_r + a_{12}k_v - \lambda k_r)e^{-\lambda\tau} + c_0 = 0\,, \tag{21}$$

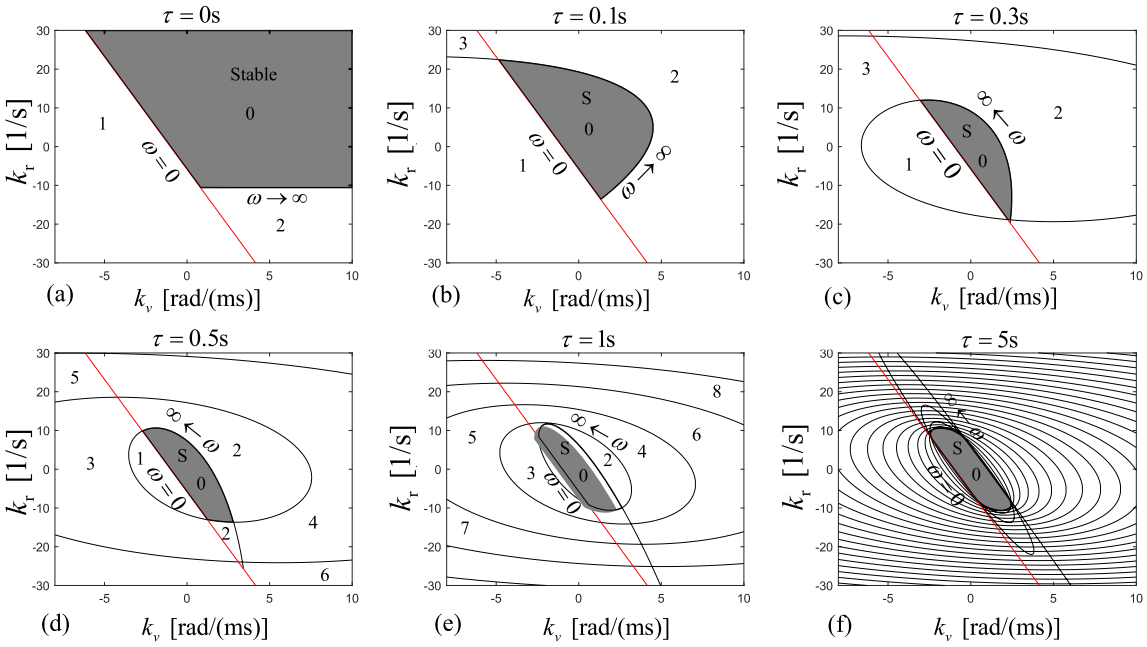

Fig. 2. The stability chart for control gains in a completely linearised model of understeer vehicle with longitudinal speed $u = 35$ m/s showing the number of unstable characteristic roots with various (even unrealistic) time delays τ: (a) 0 s, (b) 0.1 s, (c) 0.2 s, (d) 0.5 s, (e) 1 s, (f) 5 s. Shadowed areas indicate stable domains. Red lines refer to static loss of stability, black lines refer to dynamic loss of stability. (For interpretation of the references to colour in this figure legend, the reader is referred to the web version of this article.)

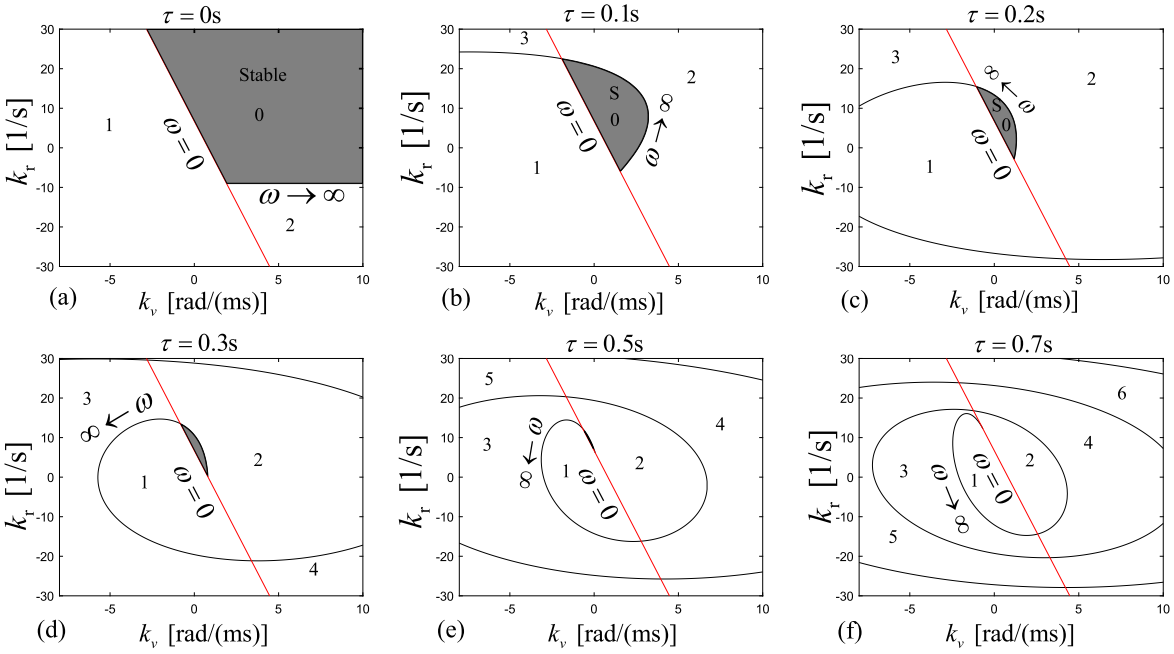

Fig. 3. The stability chart for control gains in a completely linearised model of oversteer vehicle with longitudinal speed $u = 35$ m/s showing the number of unstable characteristic roots with various time delays τ: (a) 0 s, (b) 0.1 s, (c) 0.2 s, (d) 0.3 s, (e) 0.5 s, (f) 0.7 s. Shadowed areas indicate stable domains. Red lines refer to static loss of stability, black lines refer to dynamic loss of stability. No stable parameter region exists for time delays larger than the critical delay $\tau_{cr} = 0.691$ s. (For interpretation of the references to colour in this figure legend, the reader is referred to the web version of this article.)

where $b_0 = \mathrm{Tr}\,\mathbf{A} < 0$ and $c_0 = \det \mathbf{A}$ are taken from (15).

As opposed to the characteristic polynomial (14) of the uncontrolled system, this characteristic equation $D(\lambda) = 0$ in (21) has infinitely many characteristic roots λ in the complex plane, and the necessary and sufficient condition of exponential stability is that all of them have negative real parts (see, e.g., in Breda et al. (2014)).

The so-called stability charts are constructed in the plane of certain system parameters that will be the control gains k_v and k_r in the present case. By means of the D-subdivision method (Sipahi, 2019), the D-curves (or transition curves) can be determined in the parameter plane, and the number of characteristic roots with positive real parts can be identified in the corresponding domains bounded by these curves. In case of DDEs, the structure of these curves and domains is usually intricate, and the stable ones can be identified where the number of roots with positive real parts is zero.

With reference to the D-subdivision method, the real and imaginary parts of the characteristic function are obtained by substituting $\lambda = \mathrm{i}\omega$

in the form

$$R(\omega) = -\omega^2 - (a_{11}k_r + a_{12}k_v)\cos(\omega\tau) + k_r\omega\sin(\omega\tau) + c_0 \tag{22}$$

$$S(\omega) = -b_0\omega + (a_{11}k_r + a_{12}k_v)\sin(\omega\tau) + k_r\omega\cos(\omega\tau)\,, \tag{23}$$

respectively, with $\omega \in [0, +\infty)$.

The D-curve, as a parametric function of ω, can be given by setting $R(\omega) = 0$ and $S(\omega) = 0$. This leads to the boundary of the static instability when $\omega = 0$, that is, when

$$a_{11}k_r + a_{12}k_v = c_0\,, \tag{24}$$

while it leads to the boundary of the dynamic instability when $\omega > 0$, that is, when

$$k_v(\omega) = \frac{1}{a_{12}\omega}\left((c_0 - \omega^2 - a_{11}b_0)\omega\cos(\omega\tau) + (a_{22}\omega^2 + a_{11}c_0)\sin(\omega\tau)\right), \tag{25}$$

$$k_r(\omega) = \frac{1}{\omega}\left((\omega^2 - c_0)\sin(\omega\tau) + (a_{11} + a_{22})\omega\cos(\omega\tau)\right). \tag{26}$$

When $\omega = 0$, the D-curve is a straight line in the parameter plane (k_v, k_r), which is denoted by red in Figs. 2 and 3. In these cases, a real critical characteristic root crosses the imaginary axis at 0 and the corresponding state of the vehicle loses its stability exponentially without vibrations in the domains where the number of unstable characteristic roots is 1, that is, to the left of the red lines.

When $\omega > 0$, the D-curves (25)–(26) spiral outwards in the parameter plane (k_v, k_r) (see the black curves in Figs. 2 and 3); a complex conjugate pair of characteristic roots $\lambda = \pm i\omega$ crosses the imaginary axis and the vehicle state loses its stability via self-excited vibrations of angular frequency ω. The above two types of D-curves split the parameter plane into infinite number of domains with finite number of unstable characteristic roots within these domains. In the stable domains (see dark grey regions in Figs. 2 and 3), this number is 0.

The number N of unstable characteristic roots is calculated by means of the formula

$$N = 1 + \sum_{k=1}^{r}(-1)^k \operatorname{sgn} S(\rho_k)\,, \tag{27}$$

where $\rho_1 \geq \cdots \geq \rho_r \geq 0$ are the positive real zeros of $R(\omega)$. This formula is a special case of the stability criterion derived in Stepan (1989) for delayed oscillators like (17).

4.2. Stability charts for the completely linearised delayed model

The geometric data a and b in Table 1 and the cornering stiffnesses of the linear tyre model given in Table 2 can directly be used as the parameters of an understeer characteristic since

$$C_f a - C_r b = -4867.3\,\text{Nm} < 0\,, \tag{28}$$

as it is shown by formula (10). The longitudinal speed is selected for the challenging large value of $u = 35\,\text{m/s}$, while the radius R of the cornering manoeuvre is considered to be large enough to satisfy the small steering angle condition in (9), which is assumed in the completely linearised model.

The stability charts in Fig. 2 are presented for this parameter setup. If there were no time delay in the stability control, the gains k_v, k_r could be increased to any large positive values (see panel (a) in Fig. 2). However, as the time delay increases, the stable region starts shrinking as shown by panels (b)–(f) in Fig. 2. Note that the stable parameter region survives even for unrealistic large delays like $\tau = 5\,\text{s}$, which is due to the fact that the understeer case is always stable in the completely linearised model even without stability control.

The oversteer characteristic is modelled by adjusting the user scaling factor λ_{Ky} in (A.4) and (A.5) (see Appendix) in a way that the cornering stiffnesses at the front and at the rear are increased and decreased by 40%, respectively, to have $C_f = 170\,490\,\text{N/rad}, C_r = 63\,486\,\text{N/rad}$, which results in

$$C_f a - C_r b = 11\,457\,\text{Nm} > 0\,. \tag{29}$$

This oversteer characteristic is used in the stability charts of Fig. 3. The longitudinal speed is the same as in the understeer case, which is chosen intentionally for

$$u = 35\,\text{m/s} > u_{cr} = 21.13\,\text{m/s} \tag{30}$$

to create unstable uncontrolled oversteer characteristic in accordance with (16).

Fig. 3 presents the corresponding stability charts. For small time delays $\tau < 0.2\,\text{s}$, the structure of the stability charts is practically the same as in the understeer case, although the stable regions get somewhat smaller as the delay increases. For even larger delays, the stable region disappears. A critical time delay τ_{cr} exists where no control gains k_v, k_r can be selected which could stabilise the system for $\tau > \tau_{cr}$. The exact value of this critical delay can be calculated by means of the tangent of the D-curve given by (25) and (26) as the angular frequency $\omega \to 0$. This tangent should be larger than the tangent of the static straight line boundary given by (24) (see the red straight line in Fig. 3):

$$\lim_{\omega\to 0}\frac{\mathrm{d}k_r}{\mathrm{d}k_v} = \lim_{\omega\to 0}\frac{\mathrm{d}k_r/\mathrm{d}\omega}{\mathrm{d}k_v/\mathrm{d}\omega} > -\frac{a_{12}}{a_{11}}\,. \tag{31}$$

This calculation results in the condition:

$$-\frac{a_{12}}{a_{11}} + \frac{-b_0\tau^2 + 2\tau}{c_0\tau^2 - 2b_0\tau + 2} > -\frac{a_{12}}{a_{11}}\,, \tag{32}$$

which leads to the necessary condition for the time delay:

$$\tau < \tau_{cr} = \frac{b_0 - \sqrt{b_0^2 - 2c_0}}{c_0} = 0.691\,\text{s}\,, \tag{33}$$

where $b_0 = \operatorname{Tr}\mathbf{A} < 0$ and also $c_0 = \det\mathbf{A} < 0$ according to the oversteer case given in (30). Consequently, no stable region exists in panel (f) of Fig. 3 where $\tau > \tau_{cr}$.

5. Delayed stability control for the non-linear vehicle model

With considerations of the non-linear tyre force and the effect of large steering angle, the structure of the non-linear equations is given as

$$\begin{bmatrix}\dot{v}\\ \dot{r}\end{bmatrix} = \begin{bmatrix}F(v,r)\\ G(v,r)\end{bmatrix}\,, \tag{34}$$

which is obtained from (1) after the substitution of the lateral tyre forces F_{fy} and F_{ry} in (3) and the slip angles in (2).

Understeer and oversteer cases are modelled by constructing the normalised tyre/axle characteristic curves of vehicle handling diagram derived in Pacejka (2005). As shown in Fig. 4, a 10% loss of tyre–road contact coefficient μ is considered by means of the reduction of the scaling factor $\lambda_{\mu y}$ in (A.2) (see Appendix) either at the front or at the rear axle relative to the maximum reference value of 1: for understeer, $\mu_f = 0.9$ and $\mu_r = 1$, while for oversteer, $\mu_f = 1$ and $\mu_r = 0.9$ are used, respectively. Accordingly, the loss of force capability at the front axle will lead to understeer as the front tyre force saturates before the rear one, while the opposite case will lead to oversteer.

The desired vehicle state (v_0, r_0) is an equilibrium point corresponding to input steering angle δ and longitudinal speed u, where the location and type of this equilibrium are accurately acquired by the means of phase portraits as conducted in Bobier-Tiu et al. (2019).

The uncontrolled system stability can be checked with the help of the linearisation of (34) at (v_0, r_0). This leads to the calculation of the eigenvalues of the Jacobian

$$\mathbf{A} = \begin{bmatrix}\left.\frac{\partial F(v,r)}{\partial v}\right|_{(v_0,r_0)} & \left.\frac{\partial F(v,r)}{\partial r}\right|_{(v_0,r_0)}\\ \left.\frac{\partial G(v,r)}{\partial v}\right|_{(v_0,r_0)} & \left.\frac{\partial G(v,r)}{\partial r}\right|_{(v_0,r_0)}\end{bmatrix} \tag{35}$$

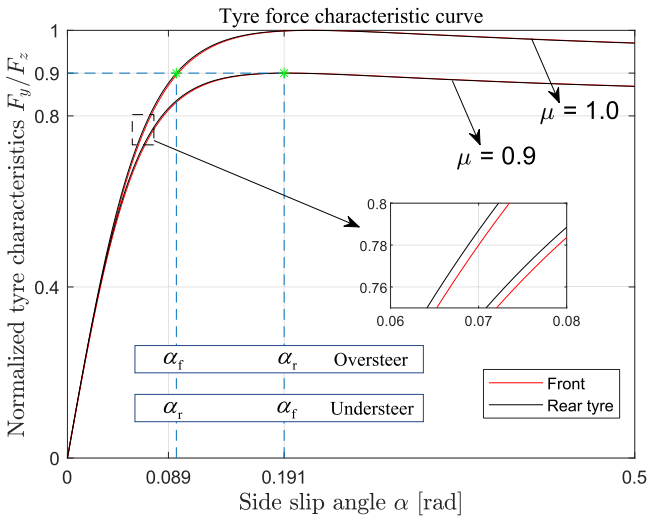

Fig. 4. Tyre force characteristic curves for different contact coefficients μ. The front and rear tyres characteristic curves (red and black curves, respectively) are slightly different even in this normalised form due to the different nonlinear dependences (A.1) and (A.2) on the vertical loads F_{fz} and F_{rz}. (For interpretation of the references to colour in this figure legend, the reader is referred to the web version of this article.)

that cannot be presented here in closed algebraic form as it was done in the completely linearised model in (13). However, checking the real parts of the eigenvalues can be done as it was presented in (14)–(16) in case of complete linearisation.

By combining the non-linear vehicle model in (34) and the stability controller with time delay in (7), the non-linear controlled dynamic model with feedback delay is

$$\begin{bmatrix}\dot v\\ \dot r\end{bmatrix} = \begin{bmatrix}F(v,r)\\ G(v,r)\end{bmatrix} + \begin{bmatrix}0\\ M_z(t)\end{bmatrix}. \tag{36}$$

To analyse the dynamics of this system, the same procedure is followed as in case of the completely linearised model, however, no closed form analytical expressions can be obtained here due to the complexity of the non-linear mathematical expressions. The equilibria (v_0, r_0) remain the same as in the uncontrolled non-linear model (34), but the linearisation at these points leads to intricate transcendental characteristic functions like (21). Still, the corresponding stability charts provide guidance for the selection of the optimal control gains in the presence of certain unavoidable time delays in the control loop, and the corresponding phase diagrams provide a clear representation of the optimised dynamics of the controlled system.

5.1. Fastest settling signals in the presence of time delay

Small initial perturbations of the vehicle system decay in the fastest way if the largest real part of the infinitely many characteristic roots has a minimal negative value:

$$\min\{\max_{k=1,2,\dots} \mathrm{Re}\lambda_k\} =: -\zeta < 0. \tag{37}$$

In this case, the state variables settle according to $e^{-\zeta t}$ where the decay rate ζ has the unit 1/s. The best robustness against the small initial perturbations can be provided by maximising the value of $\zeta > 0$ by means of the optimal selection of the control gains. This can be achieved with the analysis of the characteristic functions calculated at the desired equilibria.

The characteristic function is obtained from the linearised system like (18) where the coefficient control matrix **B** is the same as in (19), and the system coefficient matrix **A** must be substituted by the Jacobian of (36), which is the same as in case of (34). Introduce the shifted characteristic exponent

$$\hat\lambda = \lambda + \zeta, \quad \zeta > 0. \tag{38}$$

Clearly, the stability condition for $\hat\lambda$ is equivalent to the condition $\mathrm{Re}\lambda < -\zeta$. The shifted characteristic exponents $\hat\lambda$ satisfy

$$\begin{aligned} D(\hat\lambda;\zeta) := \hat\lambda^2 - (b_0 + 2\zeta)\hat\lambda - (a_{11}k_r + a_{12}k_v + \zeta k_r)e^{(\zeta-\hat\lambda)\tau} \\ + k_r\hat\lambda e^{(\zeta-\hat\lambda)\tau} + c_0 + b_0\zeta + \zeta^2 = 0, \end{aligned} \tag{39}$$

where the dependence of the characteristic function D on the decay rate ζ is also emphasised in the arguments of D.

In what follows, the stability charts are presented, and also the control gains are optimised within the stable regions for realistic time delays in a way that the decay rate ζ is maximised, that is, the controlled vehicle system settles at the desired state in the fastest way for small initial perturbations.

5.2. Stability charts and control gain optimisation for maximum decay rate in the non-linear delayed model

By repeating the same derivation for $D(\hat\lambda;\zeta)$ in (39) which was performed in the completely linearised delayed model, the static and dynamic stability boundaries can be constructed with $\zeta = 0$. The corresponding stability charts are presented in Figs. 5 and 6 where the stable domains are denoted by shaded regions. The driving inputs are selected as follows: the steering angle δ is set to 0.2 rad for understeer, and 0.1 rad for oversteer, while the longitudinal speed u is set to 15 m/s in both cases. The time delays are chosen to be the realistic values of 0.1 s, 0.2 s, 0.3 s, and some exaggerated values of 0.4 s, 0.5 s in understeer, and some extreme values of 1.5 s, 2.0 s, 3.0 s in oversteer that is clearly impossible in practice and here for completeness of theory.

Virtual static and dynamic boundaries can be calculated from (39) with $\zeta > 0$ decay rates where $\mathrm{Re}\hat\lambda < 0$, that is, where $\mathrm{Re}\lambda < -\zeta$. Within the stable domains, the grey-scale refers to these smaller and smaller regions where the decay rate ζ is larger and larger. Clearly, at a certain maximum value of ζ_{max}, the stable regions for $\hat\lambda$ will disappear, which means that no control gains can be found such that $\mathrm{Re}\lambda < -\zeta_{max}$ for all the characteristic roots λ. In other words, the optimal control gains $k_{v,\zeta}, k_{r,\zeta}$ can be calculated where the controlled non-linear system settles locally at the desired state in the fastest way against initial perturbations.

As it can be seen in Figs. 5 and 6, the maximum decay rate depends on the time delay in the control loop. For relatively small delays, it is obtained as in the completely linearised delayed model by means of (31) and (32). Accordingly, we have the condition

$$\lim_{\omega\to 0}\frac{\mathrm{d}k_r}{\mathrm{d}k_v} = \lim_{\omega\to 0}\frac{\mathrm{d}k_r/\mathrm{d}\omega}{\mathrm{d}k_v/\mathrm{d}\omega} > -\frac{a_{12}}{a_{11}+\zeta}, \tag{40}$$

where $k_v(\omega;\zeta)$ and $k_r(\omega;\zeta)$ are calculated in the same way as (25) and (26) but with the real and imaginary parts of the extended characteristic function $D(\hat\lambda;\zeta)$ in (39). This leads to the condition

$$\zeta < \zeta_{max} = \frac{1}{2\tau}\left(-\tau b_0 + 4 - \sqrt{\tau^2(b_0^2 - 4c_0) + 8}\right), \tag{41}$$

which means that the maximum available decay rate is ζ_{max} at a given value of time delay, where $b_0 = \mathrm{Tr}\,\mathbf{A} < 0$ and also $c_0 = \det\mathbf{A} > 0$ with Jacobian **A** given by (35). Nevertheless, this condition (41) exists only when

$$0 < \tau < \tau^\star := \frac{4}{\sqrt{8c_0 - 2b_0^2}}, \tag{42}$$

where $b_0^2 < 4c_0$ fulfils for the Jacobian matrix **A** with the given parameters of the vehicle. As it is shown in Fig. 7, these critical values $\tau^\star$ of the delay are at 0.3169 s for understeer that could be reached in practical cases and causing a massive decrease in system stability,

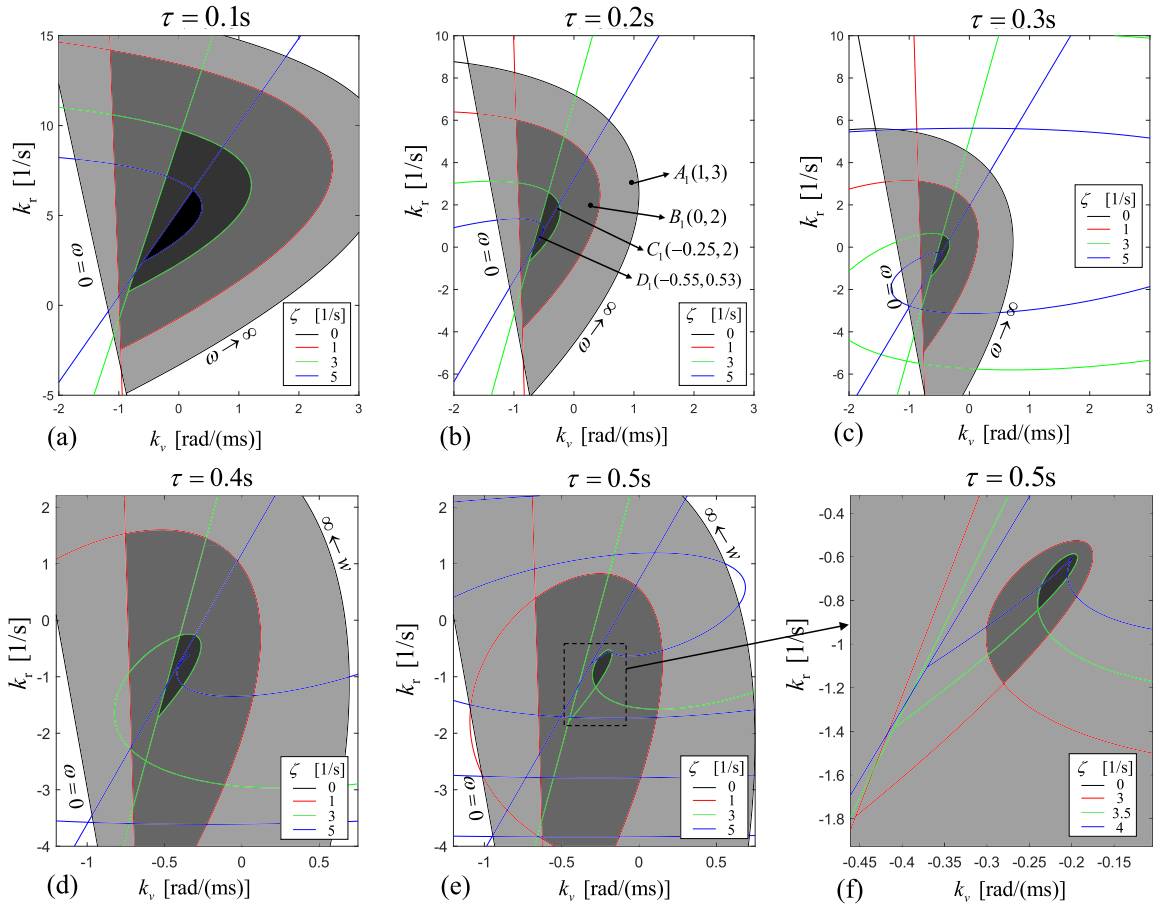

Fig. 5. Stability charts for control gains in the non-linear delayed model of understeer vehicle for $u = 15\,\mathrm{m/s}$ and $\delta = 0.2\,\mathrm{rad}$ with various time delays τ and decay rates ζ, where the grey-scale areas refer to increasing ζ and corresponding decreasing settling times. In case of the three upper panels, the maximum decay rate $\zeta_{\max}$ is given by (41): (a) 7.934 1/s, (b) 5.869 1/s, (c) 6.502 1/s, while in panel (d) and (e), $\zeta_{\max}$ is given by (44): (d) 5.444 1/s, (e) 3.987 1/s. Note the change of scales in the figures; panel (f) presents an enlarged section of panel (e).

and at 1.1373 s for oversteer meaning that practically it cannot get breached.

For time delays $\tau > \tau^\star$, the lower panels of Figs. 5 and 6 show that the achievable maximal decay rate exists within a loop of the virtual stable region. Consequently, $\zeta_{\max}$ can be calculated from the conditions

$$\frac{\mathrm{d}k_\mathrm{v}}{\mathrm{d}\omega} = 0, \quad \frac{\mathrm{d}k_\mathrm{r}}{\mathrm{d}\omega} = 0 \tag{43}$$

which lead to

$$\begin{aligned} &\frac{\sin(\tau\omega)}{\omega}\left(-b_0\zeta\tau + b_0 - c_0\tau + 2\zeta - \zeta^2\tau + \tau\omega^2\right) \\ &\quad + \cos(\tau\omega)(b_0\tau + 2\zeta\tau - 2) = 0\,, \\ &\frac{\sin(\tau\omega)}{\omega}\left(\zeta(b_0+\zeta) - \omega^2(b_0\tau + 2\zeta\tau - 1) + c_0\right) \\ &\quad - \cos(\tau\omega)\left(\zeta(b_0+\zeta) + c_0 - \omega^2\right)\tau = 0\,. \end{aligned} \tag{44}$$

These two equations define the parameter points where the virtual stability boundary curve has a peak. Eqs. (44) can be solved for $\zeta_{\max}$ and for the angular frequency ω where the system is just at the limit $\max\{\mathrm{Re}\lambda\} = -\zeta_{\max}$. The corresponding maximal decay rates are shown in Fig. 7 for $\tau > \tau^\star$.

It is counter-intuitive to observe that the fastest settling signal can be achieved by increasing time delays for $\tilde{\tau} < \tau < \tau^\star$, where $\tilde{\tau}_{\mathrm{us}} = 0.224\,\mathrm{s}$ for understeer and $\tilde{\tau}_{\mathrm{os}} = 0.793\,\mathrm{s}$ for oversteer. While the shortest time delay usually presents the best control performance, the time delay $\tau^\star$ presents an optimum point if the time delay τ cannot be set below $\tilde{\tau}$ (see Fig. 7). Similar observations can be found in Hu and Wang (2002) and Yan et al. (2019), where examples are presented for improving stability properties by increasing the time delay.

5.3. Numerical simulations with control gains optimised for fastest decay rate

For the system (36) of DDEs, numerical simulations are conducted with history functions to verify and check the control dynamics in the time domain under selected gain sets. While the system parameters are kept at the same values as in Tables 1 and 2, and the driver's inputs are the same as in case of Figs. 5(b) and 6(b) where the time delay τ is fixed at 0.2 s. Accordingly, two sets of control gains are selected: parameter points A_1, C_1, D_1 in Fig. 5(b) for understeer, and A_2, B_2, D_2 in Fig. 6(b) for oversteer.

The time history of the system state variables v and r are simulated and plotted in Fig. 8 by means of Matlab DDE23. The vehicle state before external perturbations is considered at its stable equilibrium v_0 and r_0, and the small impact-like perturbations around the steady yaw rate r_0 are introduced at the time instant $t = 0\,\mathrm{s}$:

$$\text{US:}\begin{cases} v(t) = -0.428\,\mathrm{m/s}, & t \in [-\tau, 0], \\ r(t) = 0.568\,\mathrm{rad/s}, & t \in [-\tau, 0),\ r(0) = 0.4\,\mathrm{rad/s} \end{cases}$$

$$\text{OS:}\begin{cases} v(t) = -1.343\,\mathrm{m/s}, & t \in [-\tau, 0], \\ r(t) = 0.369\,\mathrm{rad/s}, & t \in [-\tau, 0),\ r(0) = 0.5\,\mathrm{rad/s} \end{cases}$$

The setup of these perturbations corresponds to the scenarios that usually cause instability in the two types of steering characteristics as discussed in (5) and (6).

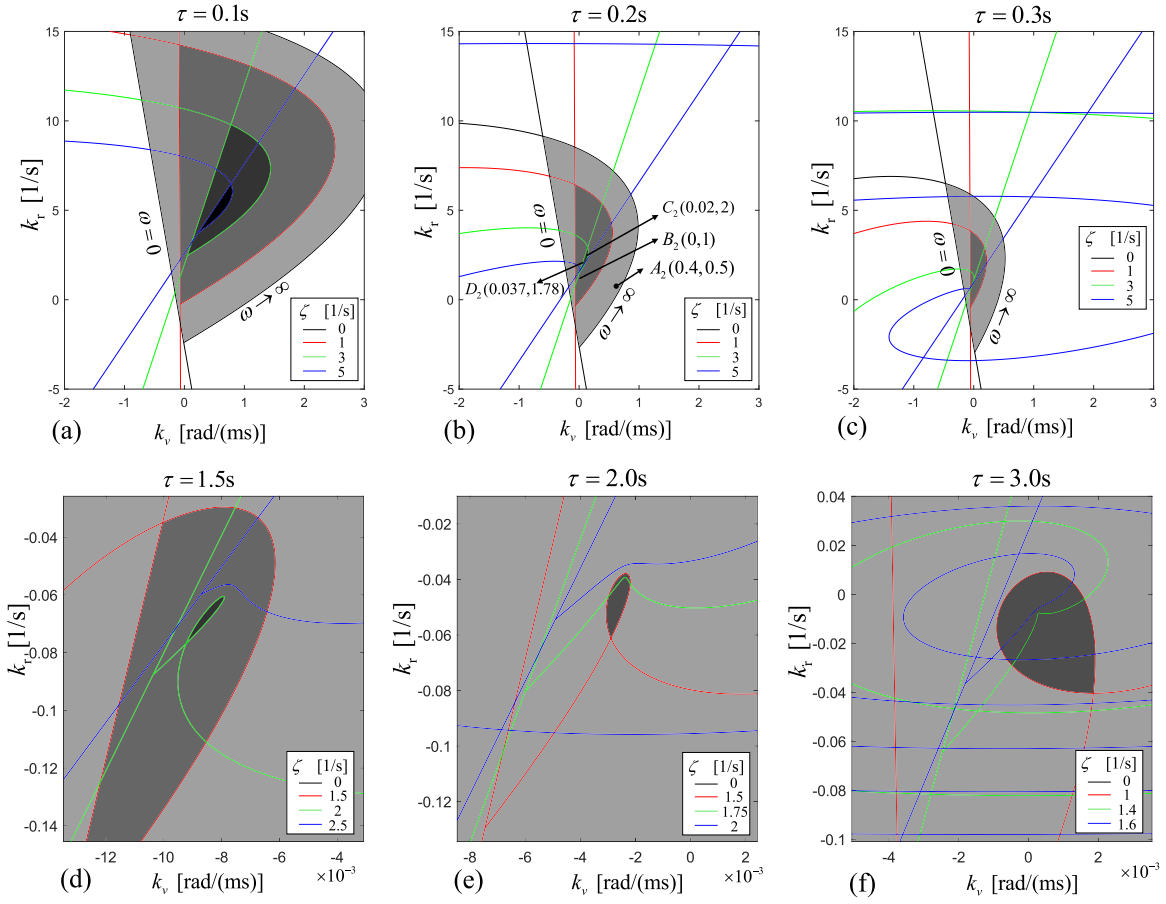

Fig. 6. Stability charts for control gains in the non-linear delayed model of oversteer vehicle for $u = 15\,\mathrm{m/s}$ and $\delta = 0.1\,\mathrm{rad}$ with various time delays τ and decay rates ζ, where the grey-scale areas refer to increasing ζ and corresponding decreasing settling times. In case of the three upper panels, the maximum decay rate $\zeta_{\max}$ is given by (41): (a) 6.977 1/s, (b) 4.103 1/s, (c) 3.184 1/s, while in panel (d), (e) and (f), $\zeta_{\max}$ is given by (44): (d) 2.111 1/s, (e) 1.656 1/s, (f) 1.363 1/s. Note the change of scales in the figures.

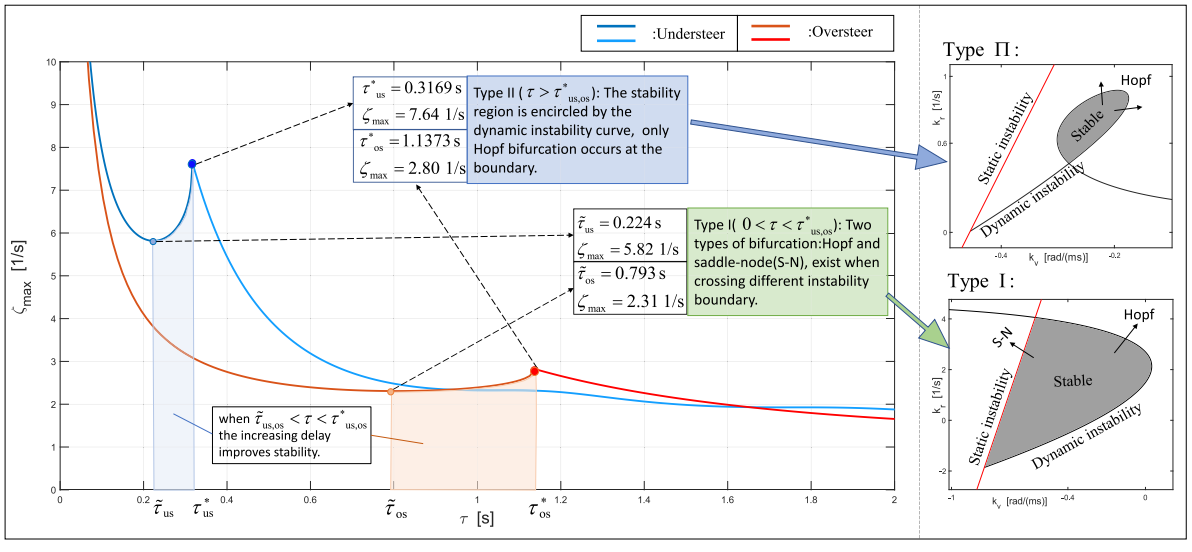

Fig. 7. The maximum available value of $\zeta_{\max}$ corresponding to the variation of time delay τ. The understeer vehicle here is encountered with $u = 15$ m/s and $\delta = 0.2$ rad, and the oversteer vehicle is driven at $u = 15$ m/s and $\delta = 0.1$ rad.

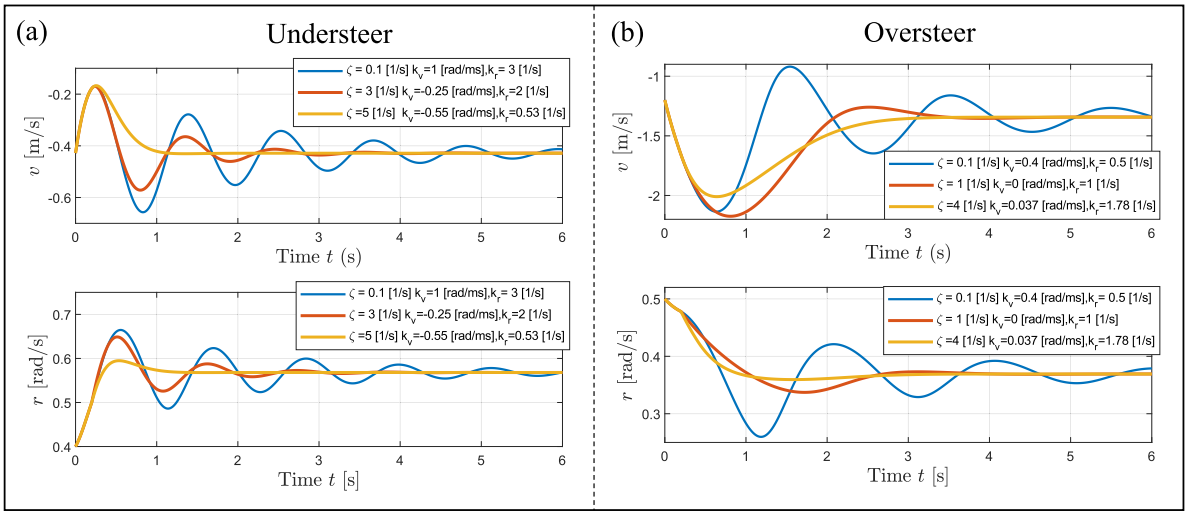

Fig. 8. Time history of system state variables v and r for $\tau = 0.2\,\mathrm{s}$ delay under different control gain configurations: (a) understeer vehicle at parameter points A_1, C_1 and D_1 in the stability chart of Fig. 5(b); (b) oversteer vehicle at parameter points A_2, B_2 and D_2 in the stability chart of Fig. 6(b).

Panel (a) in Fig. 8 presents the time history of v and r in case of understeer. Clear differences can be observed in the dynamic responses of the state variables in case of the three selected sets of gains. The system with gains at A_1 corresponds to the signals settling to the equilibrium at about 6 s after a series of state fluctuations. The settling time to the equilibrium decreases by half to 3 s with gains at C_1, and only slight vibrations are generated in this case. The gains at D_1 are close to the ζ-optimised gains $(k_{\mathrm{v},\zeta}, k_{\mathrm{r},\zeta})$ and accordingly, the signals settle the fastest way without oscillations.

The case of oversteer is presented in panel (b) of Fig. 8. The system with gains at D_2 is close to the ζ-optimised gains $(k_{\mathrm{v},\zeta}, k_{\mathrm{r},\zeta})$, and it converges to the equilibrium much faster than in the cases of control gains selected at B_2 or A_2. Note that in the ζ-optimised case, there seems to be some time lag in the response function of the lateral speed v compared to the yaw rate signal r. This can partly be explained with the small value of $k_{\mathrm{v},\zeta}$ relative to $k_{\mathrm{r},\zeta}$ and by the fact that the yaw stability control is much more crucial than the lateral speed control in oversteer vehicle.

5.4. Phase plane analysis of the non-linear delayed model

The trajectories in the phase planes (β, r) are presented in Figs. 9 and 10 for understeer and oversteer, respectively, when the same set of system parameters is used as introduced in the previous subsection for the numerical simulations with small perturbations. According to the theory of DDEs (Insperger and Stepan, 2011), the presence of the history of the state variables implies that the trajectories may cross each other in the phase plane. Still, this does not contradict to the existence and uniqueness of the solutions, it is only a consequence of the fact that the phase space of delayed systems is infinite dimensional and the phase plane represents only its two dimensional projection that still provides an appropriate overview of the global dynamic behaviour of the system.

The phase plane of the delayed system in understeer vehicle with control gains selected in Fig. 5(b) at A_1, B_1, C_1, D_1 corresponding to different decay rates ζ are plotted in panels (a), (b), (c) and (d) of Fig. 9, respectively. It can be observed that around the stable equilibria, the delayed system is getting more and more robust locally against small perturbations with the increase of the decay rate ζ. Compared to the phase planes of the uncontrolled understeer dynamics presented in Bobier-Tiu et al. (2019), the spiralling of the trajectories of small perturbations with the control gain set A_1 still results in a long recovery time of the desired vehicle state, but it is increasingly better with the gain sets B_1 and C_1, while the oscillations almost fully disappear at D_1.

However, in this understeer case, two new unstable saddle points appear in the global phase plane when the control gains are selected at C_1 and D_1. The existence of these two unstable points destroys the global stability of the understeer vehicle, and it essentially shrinks the domain of attraction of the desired state. With the increasing decay rate ζ in Fig. 9(c,d), the saddle point, having the same yaw rate as that of the stable state, starts getting closer and closer to the desired state, which makes it very sensitive even for small perturbations and the corresponding cornering manoeuvre is likely to fail. The reason why the control gains can cause the loss of global stability under large perturbations in understeer vehicle will be discussed in the next section.

The case of oversteer vehicle is presented in panels (a), (b), (c) and (d) of Fig. 10 with control gains selected in Fig. 6(b) at A_2, B_2, C_2 and D_2, respectively. Compared to the phase planes of the uncontrolled oversteer dynamics presented in Bobier-Tiu et al. (2019), the most relevant observation is that the two unstable saddle points disappear and the controlled oversteer vehicle becomes globally stable. As it can be seen in Fig. 10, the globally stable spiral point gradually turns into a stable node with the increase of the decay rate ζ from 0 to 4 1/s, which means that the system converges globally to the desired state without vibrations within a short recovery time.

5.5. Control gain optimisation for global stability

As it is shown in Fig. 9 for understeer cases, the domain of attraction shrinks as the decay rate ζ increases. Accordingly, the control gains must be optimised by keeping the balance between global stability and fast signal decay.

In order to estimate the size of the domain of attraction around the desired stable equilibrium, introduce the measure

$$\epsilon = \ln|\beta_{\mathrm{s}} - \beta_{\mathrm{u}}|\,, \tag{45}$$

where β_{s} denotes the side slip angle of the stable point S, and β_{u} denotes the side slip angle of the unstable saddle point U having approximately the same positive yaw rate as the desired stable point (see Fig. 9(c,d)).

For an understeer vehicle with time delay $\tau = 0.2\,\mathrm{s}$, Fig. 11 presents an overview of the different ϵ-levels of the domains of attraction in the plane of the control gains $(k_{\mathrm{v}}, k_{\mathrm{r}})$ where the different ζ-levels of the decay rate are also visualised. The optimal control gains that guarantee global stability and best decay rate are located at the grazing point of the green area I and the green D-curve with $\zeta = 2.1$ 1/s. This globally optimised point is found at $k_{\mathrm{v,opt}} = -0.02\,\mathrm{rad/(ms)}$, $k_{\mathrm{r,opt}} = 2.12$ 1/s. The corresponding phase plane is plotted at the right bottom panel of

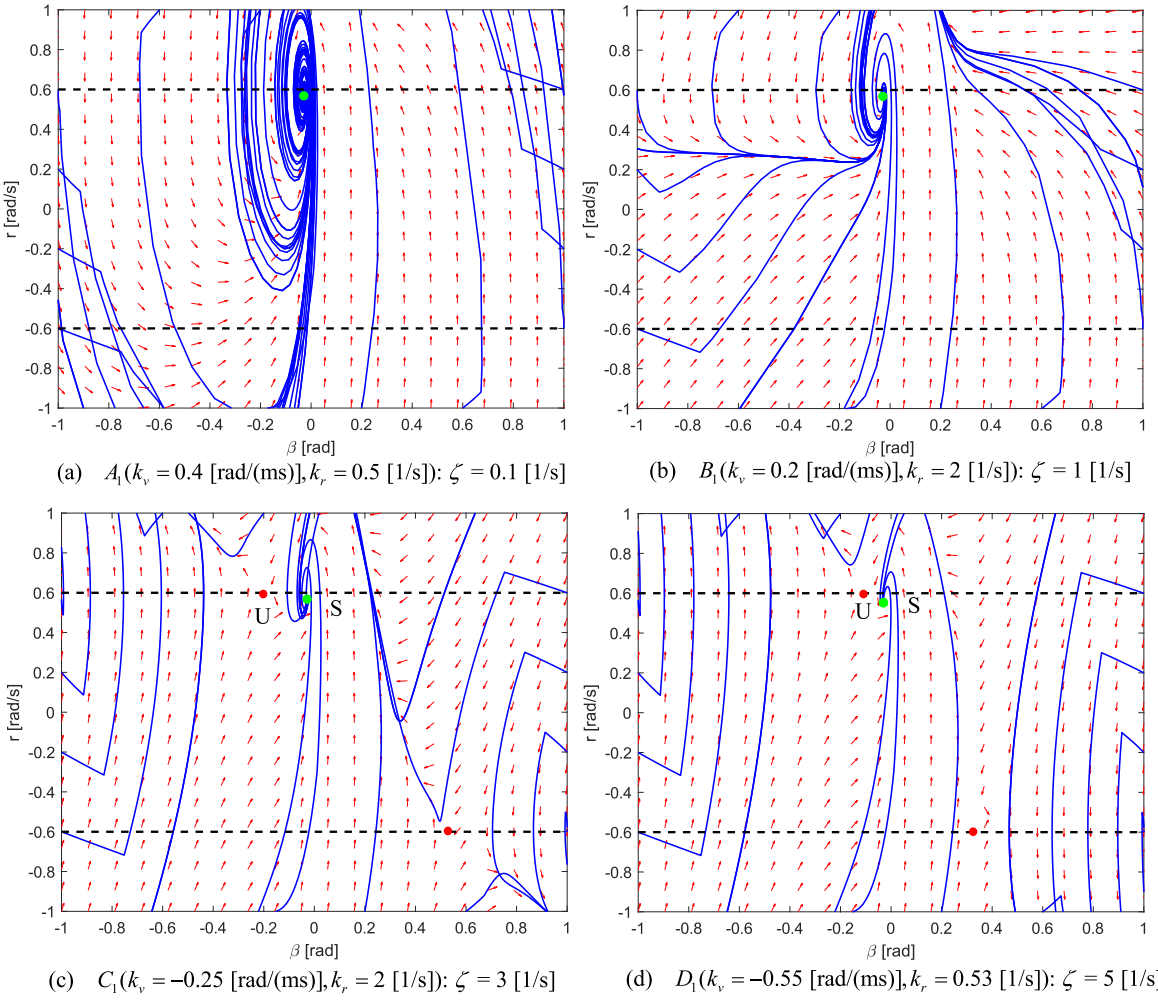

(a) $A_1(k_v = 0.4\ \text{[rad/(ms)]}, k_r = 0.5\ \text{[1/s]})$: $\zeta = 0.1\ \text{[1/s]}$

(b) $B_1(k_v = 0.2\ \text{[rad/(ms)]}, k_r = 2\ \text{[1/s]})$: $\zeta = 1\ \text{[1/s]}$

(c) $C_1(k_v = -0.25\ \text{[rad/(ms)]}, k_r = 2\ \text{[1/s]})$: $\zeta = 3\ \text{[1/s]}$

(d) $D_1(k_v = -0.55\ \text{[rad/(ms)]}, k_r = 0.53\ \text{[1/s]})$: $\zeta = 5\ \text{[1/s]}$

Fig. 9. The delayed phase plane of vehicle system with understeer characteristics at $u = 15$ m/s, $\mu_f = 0.9$, $\mu_r = 1$, $\delta = 0.2$ rad, under different control gains configurations at parameter points A_1, B_1, C_1 and D_1 in the stability chart of Fig. 2(b), respectively. Lines of maximum steady-yaw rate are drawn as black dotted lines, with variable trajectories as blue curved lines. Green dot means stable equilibrium (spiral), red dots refer to unstable equilibria (saddles), the trajectories appear as blue lines. (For interpretation of the references to colour in this figure legend, the reader is referred to the web version of this article.)

Fig. 11 which shows the result of the trade-off between global stability and fastest decay rate.

Note that global stability seems to be ensured when the stability control of the oversteer vehicle is optimised for the decay rate ζ (see Fig. 10). As the numerical results show, there are no other equilibria apart from the stable spiral/node, and there is no trace of any other attractor in the phase space. This can also be explained physically by the fact that the ζ-optimised control gains are obtained at positive values of gain k_v that helps to produce the required negative control torque as explained by formula (6). On the contrary, the ζ-optimised negative gains k_v somewhat deteriorate the global stability of the uncontrolled understeer vehicle as shown by formula (5), although they help to reduce the many large oscillations of the uncontrolled understeer vehicles in case of large steering angles δ.

6. Conclusions

This paper presents the analysis of the effect of time delay on vehicle stability control systems, and the control gains are also optimised in the presence of realistic time delays. A standard 2-dimensional vehicle handling model is established with the experimentally fitted PAC-2002 tyre model and the parameters of an SUV car.

A fully linearised model is considered first with small steering angles where simple closed form expressions can be obtained and the methodology of the stability analysis of the delayed system is introduced. This is then extended to the non-linear model both for understeer and oversteer cornering manoeuvres.

After the construction of the stability charts in the plane of the control gains, ζ-optimisation is carried out to provide the maximal achievable decay rate ζ_{max}, that is, to achieve the shortest settling time to the desired state. The phase space analysis of the delayed non-linear system provides information about the domain of attraction of the desired states. As the final step of control gain optimisation, the trade-off between decay rate maximisation and global stability is presented, which is an especially relevant issue in case of controlled understeer vehicles.

The main conclusions are summarised as follows.

1. The incorporation of realistic time delays in the model of vehicle stability control draws the attention to the essential effect of the delay on the dynamic performance of VSC: the stable control parameter region shrinks with increasing time delay. While in understeer cases, there always exist control parameter combinations that provide stability for any large delay (see Figs. 2 and 5), there exists a critical time delay τ_{cr} for oversteer vehicles above which no stable control parameter region can be found

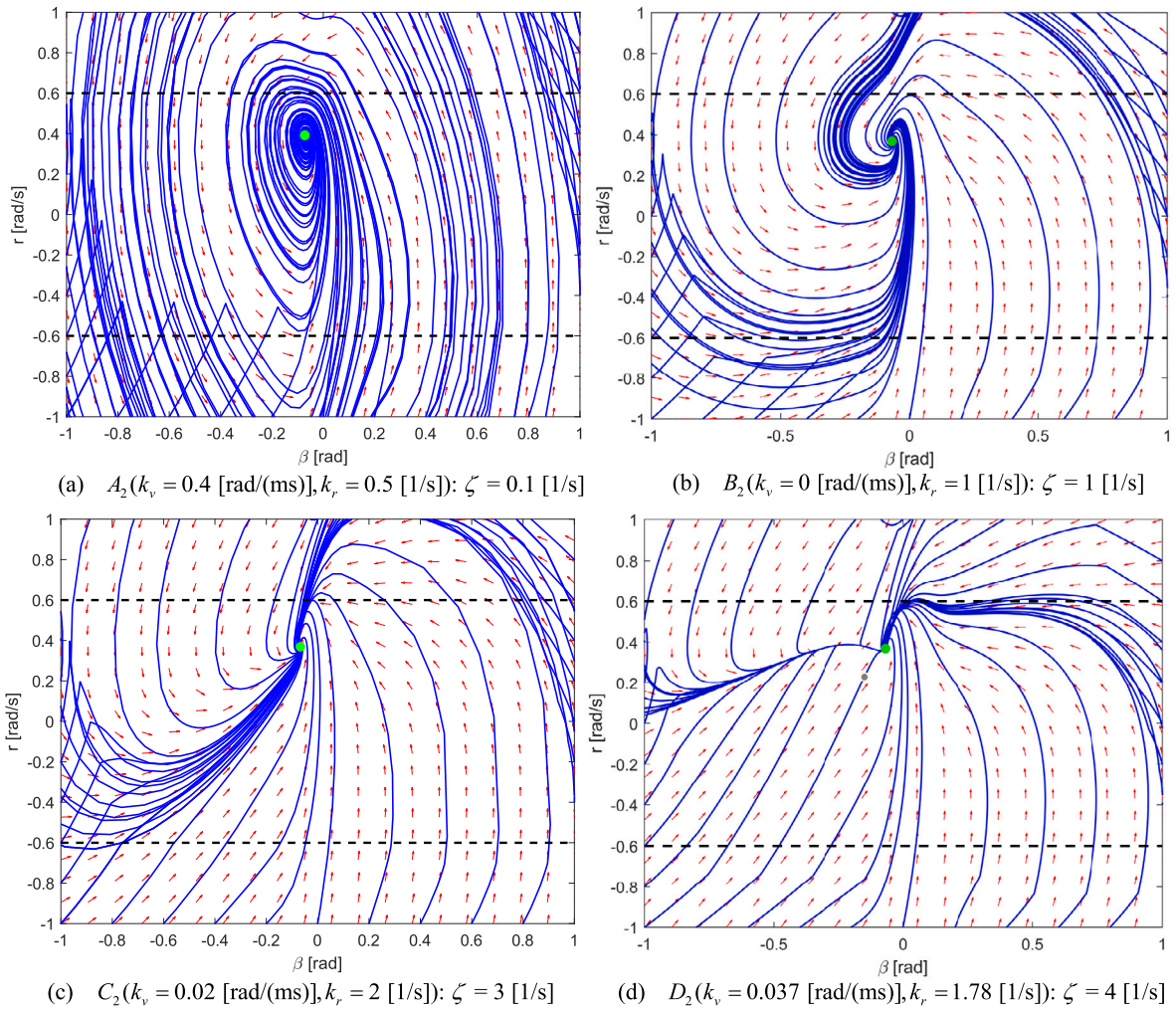

Fig. 10. The delayed phase plane of vehicle system with oversteer characteristics at $u = 15$ m/s, $\mu_f = 1$, $\mu_r = 0.9$, $\delta = 0.1$ rad, under different control gains configurations at parameter points A_2, B_2, C_2 and D_2 in the stability chart of Fig. 6(b) respectively. Lines of maximum steady-yaw rate are drawn as black dotted lines, with variable trajectories as blue curved lines. Green dot means stable equilibrium (node or spiral), red dots refer to unstable equilibria (saddles), the trajectories appear as blue lines. (For interpretation of the references to colour in this figure legend, the reader is referred to the web version of this article.)

(see Fig. 3). In case of small steering angles, this critical delay is calculated with the tyre and vehicle parameters in formula (33) with (15) as a function of the longitudinal speed u.

2. The analysis of the non-linear model shows that two types of stable regions occur in the plane of the control gains depending on whether the time delay τ is smaller or larger than the boundary value $\tau^\star$ in (42). In the first case of $\tau < \tau^\star$, the stable region is bounded by the static instability on one side and by the dynamic instability on the other side, while in the second case of $\tau > \tau^\star$, it is bounded by a loop of the dynamic instability only (see Figs. 5 and 6). At the parameter points where the dynamic instability boundary has a self-intersection, self-excited quasi-periodic vibrations may appear with two frequency components which may be a realistic scenario for understeer vehicles with delay $\tau^\star$ in the range of 0.3 s.
3. Based on the extended analysis of the stability charts, ζ-optimised control gains are determined where the vehicle reaches the desired state with maximal decay rate $\zeta_{\max}$. These optimal decay rates are calculated as a function of the time delay in the control loop. While the general tendency of increasing delay resulting in decreasing maximal decay rate is experienced in Fig. 7, the counter-intuitive opposite tendency also appears in a certain narrow delay interval $(\tilde{\tau}, \tau^\star)$. The corresponding diagrams in Fig. 7 help the tuning of the control parameters with taking into account the unavoidable time delay.
4. The effect of ζ-optimised gains on the non-linear delayed model is verified by numerical simulations (see the time histories in Fig. 8, and the phase planes in Figs. 9 and 10). The analyses of the phase plane trajectories show that the global stability of the oversteer vehicle can be achieved under ζ-optimised gains, while in understeer case, the global stability is destroyed with the application of the ζ-optimised gains. By means of the introduction of the measure (45) for the domain of attraction of the desired steering manoeuvres, the global optimisation of the gains is further conducted to find the fastest decay rate while also ensuring global stability in the presence of time delay.

There are several future plans to continue this research. Since the tyre and vehicle body parameters are all experimentally well identified, the VSC strategies in the presence of different time delays caused by the application of different computation and signal filtering strategies can also be tested and the gain optimisation results could be verified. Also, the influence of load transfer in vertical directions and the effect of braking/accelerating in longitudinal directions could be investigated by further extending the bicycle model applied here.

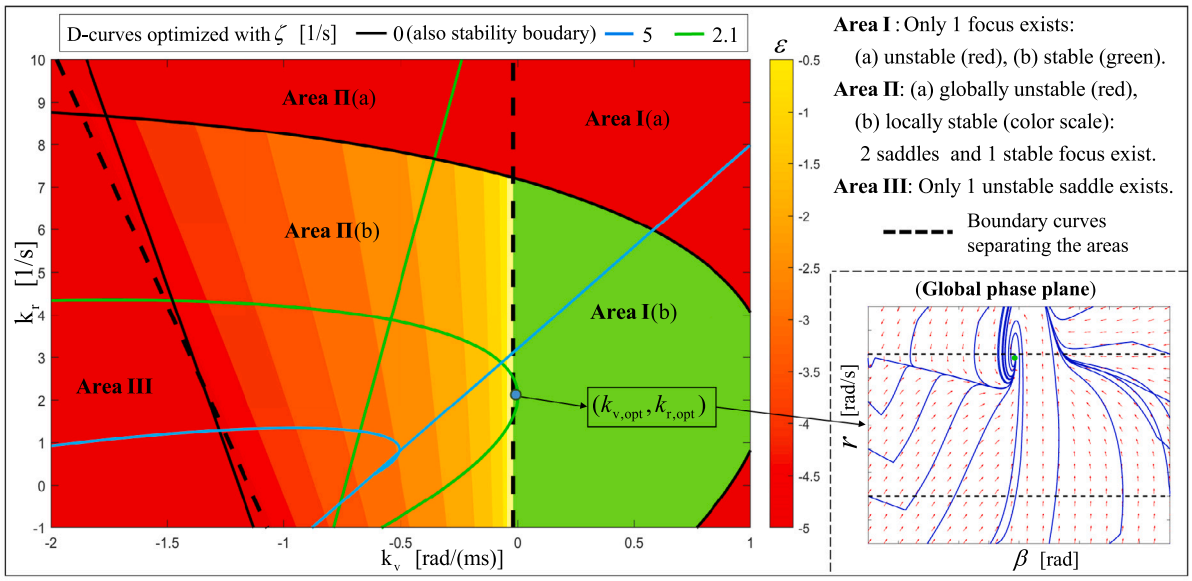

Fig. 11. Control parameter optimisation for global stability in case of understeer vehicle with delay $\tau = 0.2$ s. Deep red regions refer to global instability, green region is globally stable, and the yellow–red colour scale refers to the measure ϵ (45) of the domains of attraction in locally stable cases. The selected gains $k_{v,opt}$ and $k_{r,opt}$ are optimised by the D-curves of decay rate ζ-levels within the globally stable area, and the corresponding phase plane is given in the bottom right panel. (For interpretation of the references to colour in this figure legend, the reader is referred to the web version of this article.)

CRediT authorship contribution statement

Hangyu Lu: Methodology, Calculations, Software, Figures. **Gabor Stepan:** Conceptualization, Writing. **Jianwei Lu:** Funding acquisition, Consultancy. **Denes Takacs:** Funding acquisition, Discussion.

Declaration of competing interest

The authors declare that they have no known competing financial interests or personal relationships that could have appeared to influence the work reported in this paper.

Funding

This work was supported by the bilateral Research Project between China and Hungary Governments [grant no. 2020-1.2.4-TÉT-IPARI-2021-00012]; National Key Research and Development Project of China [grant no. 2021YFE0116600]; National Natural Science Foundation of China [grant no. 51875150]; and partly by the National Research, Development and Innovation Office of Hungary [grant no. NKFI-128422, KKP 133846, and K 132477].

Appendix. Non-linear tyre models with experimentally identified parameters

The definitions of the coefficients of the tyre model in (3) are as follows:

$$\gamma_y = \gamma\lambda_{\gamma y}\,, \quad \mathrm{d}f_z = \frac{F_z - F_{z0}}{F_{z0}}\,, \quad C_y = p_{Cy1}\lambda_{Cy}\,, \tag{A.1}$$

$$D_y = \mu F_z \xi_2\,, \quad \mu = (p_{Dy1} + p_{Dy2}\mathrm{d}f_z)(1 - p_{Dy3}\gamma_y^2)\lambda_{\mu y}\,, \tag{A.2}$$

$$E_y = (p_{Ey1} + p_{Ey2}\mathrm{d}f_z)\big(1 - (p_{Ey3} + p_{Ey4}\gamma_y)\mathrm{sgn}(\alpha)\big)\lambda_{Ey}\,, \tag{A.3}$$

while the stiffness factors are calculated as

$$K_{y0} = p_{Ky1}F_{z0}\sin\Big(2\lambda_{F_{z0}}\arctan\frac{F_z}{p_{Ky2}F_{z0}\lambda_{F_{z0}}}\Big)\lambda_{Ky}\,, \tag{A.4}$$

$$K_y = K_{y0}(1 - p_{Ky3}|\gamma_y|)\xi_3\,, \quad B_y = K_y/(C_yD_y)\,, \tag{A.5}$$

Table 2
Identified tyre parameters that are relevant in the current dynamic model.

Parameter	Value	Parameter	Value
p_{Cy1}	1.267511	p_{Ey3}	0.1150635
p_{Dy1}	0.900306	p_{Ey4}	−6.953865
p_{Dy2}	0.16748	p_{Ky1}	−25.738824
p_{Dy3}	−0.431849	p_{Ky2}	3.27049
p_{Ey1}	−0.346205	p_{Ky3}	−0.005365
p_{Ey2}	−0.10367	$p_{H\_,V\_}$	–
F_{z0} [N]	4500	γ [rad]	0.04
C_f [N/rad]	121778	C_r [N/rad]	105810

where the normal vertical load F_{z0} and the camber angle γ are used during the experimental identification. These values and the further experimentally identified tyre parameters $p_{...}$ are given in Table 2. The factors $\xi_{...}$ and $\lambda_{...}$ are used for user scaling, their default values are 1. The so-called shift factors are not presented here, they are considered to be zeros. The tyre–road contact coefficient μ is identified during the experimental tests as a general reference value that is about 1, and later it is adjusted by the user scaling factor $\lambda_{\mu y}$ to create different tyre force characteristics for the front and the rear tyres in order to simulate (non-linear) understeer or oversteer cases.

References

Acosta, M., Kanarachos, S., Blundell, M., 2018. Virtual tyre force sensors: An overview of tyre model-based and tyre model-less state estimation techniques. Proc. Inst. Mech. Eng. D 232 (14), 1883–1930.

Bobier-Tiu, C.G., Beal, C.E., Kegelman, J.C., Hindiyeh, R.Y., Gerdes, J.C., 2019. Vehicle control synthesis using phase portraits of planar dynamics. Veh. Syst. Dyn. 57 (9), 1318–1337.

Boussaada, I., Niculescu, S.-I., El-Ati, A., Pérez-Ramos, R., Trabelsi, K., 2020. Multiplicity-induced-dominancy in parametric second-order delay differential equations: Analysis and application in control design. ESAIM Control Optim. Calc. Var. 26, 57.

Breda, D., Maset, S., Vermiglio, R., 2014. Stability of Linear Delay Differential Equations: A Numerical Approach with MATLAB. Springer.

Chen, Y., Ji, Y., Guo, K., 2014. A reduced-order nonlinear sliding mode observer for vehicle slip angle and tyre forces. Veh. Syst. Dyn. 52 (12), 1716–1728.

Doumiati, M., Victorino, A., Charara, A., Lechner, D., 2011. Estimation of road profile for vehicle dynamics motion: experimental validation. In: Proceedings of the 2011 American Control Conference. IEEE, pp. 5237–5242.

Goh, J.Y., Goel, T., Gerdes, J.C., 2019. Toward automated vehicle control beyond the stability limits: Drifting along a general path. J. Dyn. Syst. Meas. Control 142 (2), http://dx.doi.org/10.1115/1.4045320.

Horvath, A., Beda, P., Takacs, D., 2021. Modelling and stability analysis of a longitudinal wheel dynamics control loop with feedback delay. Veh. Syst. Dyn. 1–23.

Hu, H.Y., Wang, Z.H., 2002. Dynamics of Controlled Mechanical Systems with Delayed Feedback. Springer Science & Business Media.

Insperger, T., Stepan, G., 2011. Semi-Discretization for Time-Delay Systems: Stability and Engineering Applications. vol. 178, Springer Science & Business Media.

Kuiper, E., Van Oosten, J., 2007. The PAC2002 advanced handling tire model. Veh. Syst. Dyn. 45 (S1), 153–167.

Lugner, P., 2019. Vehicle Dynamics of Modern Passenger Cars. Springer.

Miller, J.I., Cebon, D., 2013. An investigation of the effects of pneumatic actuator design on slip control for heavy vehicles. Veh. Syst. Dyn. 51 (1), 139–164.

Nam, K., Oh, S., Fujimoto, H., Hori, Y., 2011. Vehicle state estimation for advanced vehicle motion control using novel lateral tire force sensors. In: Proceedings of the 2011 American Control Conference. IEEE, pp. 4853–4858.

Oh, S., Avedisov, S.S., Orosz, G., 2021. On the handling of automated vehicles: Modeling, bifurcation analysis, and experiments. Eur. J. Mech. A Solids 90, 104372. http://dx.doi.org/10.1016/j.euromechsol.2021.104372.

Olofsson, B., Nielsen, L., 2021. Using crash databases to predict effectiveness of new autonomous vehicle maneuvers for lane-departure injury reduction. IEEE Trans. Intell. Transp. Syst 22 (6), 3479–3490. http://dx.doi.org/10.1109/TITS.2020.2983553.

Orosz, G., Stepan, G., 2006. Subcritical hopf bifurcations in a car-following model with reaction-time delay. Proc. R. Soc. A: Mathematical, Physical and Engineering Sciences 462 (2073), 2643–2670.

Pacejka, H., 2005. Tire and Vehicle Dynamics. Elsevier.

Patole, S.M., Torlak, M., Wang, D., Ali, M., 2017. Automotive radars: A review of signal processing techniques. IEEE Signal Process. Mag. 34 (2), 22–35.

Pi, D., Chen, N., Zhang, B., 2011. Experimental demonstration of a vehicle stability control system in a split-μ manoeuvre. Proc. Inst. Mech. Eng. D 225 (3), 305–317.

Rossa, F.D., Mastinu, G., 2017. Analysis of the lateral dynamics of a vehicle and driver model running straight ahead. Nonlinear Dynam. 92 (1), 97–106. http://dx.doi.org/10.1007/s11071-017-3478-1.

Rossa, F.D., Mastinu, G., Piccardi, C., 2012. Bifurcation analysis of an automobile model negotiating a curve. Veh. Syst. Dyn. 50 (10), 1539–1562.

Singh, K.B., Arat, M.A., Taheri, S., 2018. Literature review and fundamental approaches for vehicle and tire state estimation. Veh. Syst. Dyn..

Sipahi, R., 2019. Mastering Frequency Domain Techniques for the Stability Analysis of LTI Time Delay Systems. vol. 20, SIAM.

Sipahi, R., Atay, F.M., Niculescu, S.-I., 2008. Stability of traffic flow behavior with distributed delays modeling the memory effects of the drivers. SIAM J. Appl Math 68 (3), 738–759. http://dx.doi.org/10.1137/060673813.

Sridhar, N., Devika, K., Subramanian, S.C., Vivekanandan, G., Sivaram, S., 2021. Antilock brake algorithm for heavy commercial road vehicles with delay compensation and chattering mitigation. Veh. Syst. Dyn. 59 (4), 526–546.

Stepan, G., 1989. Retarded Dynamical Systems: Stability and Characteristic Functions. Longman Scientific & Technical.

Takacs, D., Stepan, G., 2012. Micro-shimmy of towed structures in experimentally uncharted unstable parameter domain. Veh. Syst. Dyn. 50 (11), 1613–1630.

Takahashi, J., Yamakado, M., Saito, S., Yokoyama, A., 2012. A hybrid stability-control system: combining direct-yaw-moment control and G-vectoring control. Veh. Syst. Dyn. 50 (6), 847–859.

Várszegi, B., Takacs, D., Orosz, G., 2019. On the nonlinear dynamics of automated vehicles – A nonholonomic approach. Eur. J. Mech. A Solids 74, 371–380. http://dx.doi.org/10.1016/j.euromechsol.2018.11.015.

Verma, R., Ginoya, D., Shendge, P., Phadke, S., 2015. Slip regulation for anti-lock braking systems using multiple surface sliding controller combined with inertial delay control. Veh. Syst. Dyn. 53 (8), 1150–1171.

Wang, Q., Wang, Z., 2017. Optimal feedback gains of a delayed proportional-derivative (PD) control for balancing an inverted pendulum. Acta Mech. Sinica 33 (3), 635–645.

Wu, X., Zhang, M., Xu, M., 2019. Active tracking control for steer-by-wire system with disturbance observer. IEEE Trans. Veh. Technol 68 (6), 5483–5493. http://dx.doi.org/10.1109/TVT.2019.2910540.

Xu, S., Peng, H., Tang, Y., 2021. Preview path tracking control with delay compensation for autonomous vehicles. IEEE Trans. Intell. Transp Syst 22 (5), 2979–2989. http://dx.doi.org/10.1109/TITS.2020.2978417.

Yan, G., Fang, M., Xu, J., 2019. Analysis and experiment of time-delayed optimal control for vehicle suspension system. J. Sound Vib. 446, 144–158.

Zhao, W., Qin, X., Wang, C., 2018. Yaw and lateral stability control for four-wheel steer-by-wire system. IEEE/ASME Trans. Mechatronics 23 (6), 2628–2637.